J. Synchrotron Rad. (1999). **6**, 69–80

Scanning X-ray spectrometer for high-resolution Compton profile measurements at ESRF

P. Suortti,[a]*† T. Buslaps,[a] P. Fajardo,[a] V. Honkimäki,[a] M. Kretzschmer,[a] U. Lienert,[a] J. E. McCarthy,[a] M. Renier,[a] A. Shukla,[a] Th. Tschentscher[a]‡ and T. Meinander[b]

[a]*European Synchrotron Radiation Facility, BP 220, F-38043 Grenoble CEDEX, France, and* [b]*Technical Research Center, FIN-02150 Espoo, Finland. E-mail: suortti@esrf.fr*

(*Received 20 July 1998; accepted 5 January 1999*)

A scanning-type crystal spectrometer for high-resolution Compton profile measurements has been constructed at the High Energy Inelastic Scattering Beamline (ID15B) of the ESRF. Radiation from a seven-period asymmetrical permanent-magnet wiggler or from a superconducting wavelength shifter is focused horizontally onto the sample by a bent-crystal monochromator. Typical energies are 30, 50 and 60 keV, the flux on the sample is 10^{12} photons s^{-1}, and the relative energy bandwidth is 3×10^{-4}. The spectrometer operates in the Rowland circle geometry, where the sample is fixed and the cylindrically bent analyser crystal and the detector move on the focusing circle by synchronized translations and rotations. The main detector is a large-diameter NaI scintillation counter, the incident beam is monitored by an Si diode, and scattering from the sample is detected using a Ge detector. The recorded spectrum is corrected for the energy-dependent response of the spectrometer, background and multiple scattering, and converted to the momentum scale. The resolution of the spectrometer is calculated from the geometrical factors and the reflectivity curve of the analyser crystal, and the result is checked against the widths of the elastically scattered line and fluorescent lines. So far, 0.1 a.u. resolution in electron momentum has been achieved. The typical average count rate over the Compton profile is about 1000 counts s^{-1} from a weakly absorbing sample.

Keywords: Compton scatterings; X-ray spectrometers.

1. Introduction

It was very shortly after the initial discovery by A. H. Compton when it was realised that the electron momentum prior to the scattering event should cause a Doppler broadening of the Compton line. It was suggested by J. W. M. DuMond that the Doppler broadening could be used for studies of electronic states of atoms, and he built the first Compton spectrometer in the late 1920s. This was soon developed into a focusing spectrometer, based on the principle that is now called Cauchois geometry. There were 50 small calcite crystals on the Rowland circle orientated to reflect a given energy at one point on the opposite side of the Rowland circle. The radiation reflected by the analyser crystals was recorded on photographic film and read out by a microphotometer. These measurements gave clear evidence for the correctness of the Sommerfeld picture of free electrons in metals. This early work has been reviewed by DuMond (1933).

Focusing by bent crystals was demonstrated in the early 1930s (Johann, 1931; Cauchois, 1932; Johansson, 1933), but Compton spectrometers built on these principles were realised much later. This was mostly due to the lack of large single crystals that could be bent uniformly, the only exception being quartz. When Compton profile studies were revived in the 1960s (Cooper *et al.*, 1965; Cooper & Leake, 1967; Phillips & Weiss, 1968), scanning spectrometers with flat mosaic crystals of LiF and Soller slits were used. With the sealed X-ray tubes of that time, the count rate from a light element sample was of the order of 1 count s^{-1}, and the resolution in electron momentum was 0.2–0.3 a.u. The incident energies were limited to below 22 keV (Ag $K\alpha$ lines) and this, together with the low count rates, made Compton profile studies with crystal spectrometers obsolete when strong γ-ray sources and intrinsic Ge detectors became commercially available (Eisenberger & Reed, 1972; Manninen *et al.*, 1974; Weyrich, 1975). The incident energies extended from 60 keV (Am-241) to 660 keV (Cs-137), and compounds with any elemental composition could be studied. A Compton profile of sufficient statistical accuracy could be recorded in one week, and the resolution of 0.6–0.4 a.u. was sufficient in many applications. This is a mature method, which is still being used at several laboratories.

Improved theoretical calculations of momentum wavefunctions emphasized the need for high-resolution

† Present address: Department of Physics, PO Box 9, FIN-00014 University of Helsinki, Finland.
‡ Present address: HASYLAB/DESY, Notkestrasse 85, D-22603 Hamburg, Germany.

Compton profile measurements. Compton profile studies have a special place in the testing of theoretical calculations. If the incident energy is high enough for the impulse approximation to hold, the electronic ground state is probed directly. Differences between Compton profiles corresponding to different crystallographic directions and discontinuities of the derivative of the profile reveal details of the Fermi surface. Angular correlation of photons produced in positron annihilation may yield the electron momentum with better accuracy, but there are potential complications due to the positron wavefunction and crystal defects. DeHaas–vanAlphen measurements require crystals of good quality and are performed at low temperatures, so that the field of applications is limited. However, Compton profile measurements could be competitive with these methods if the resolution was improved to 0.1 a.u.

The first Compton spectrometers at synchrotron radiation sources were built at LURE (Loupias & Petiau, 1980) and HASYLAB (Berthold *et al.*, 1992). Both spectrometers are based on the use of Cauchois geometry, where the beam from a double-crystal monochromator is collimated on the sample, which is outside the focusing circle of the instrument. An Si crystal is bent to the diameter of the focusing circle, and a position-sensitive detector (proportional counter or Ge-strip detector) is placed on the opposite side of the focusing circle. The incident energy is relatively low in both cases, less than 20 keV at LURE and 32 keV at HASYLAB, and typical count rates are 100 counts s^{-1} and typical resolutions are 0.15 a.u. Another Cauchois-type spectrometer has been built at KEK, Japan (Sakurai *et al.*, 1992). It has four analyser crystals and image plates as detectors. The incident energy is 40–70 keV and the resolution is $\sim$0.1 a.u. The attractive feature of Cauchois geometry is that the whole spectrum is recorded simultaneously, so that beam monitoring is not needed, but this advantage is offset by a rather high background and need of careful calibration of the position-sensitive detector.

A systematic study for the design of an optimized scanning spectrometer was initiated by one of the present authors (Suortti *et al.*, 1986*a*,*b*). The first spectrometer was built to operate with a sealed X-ray tube, and it was shown that a perfect crystal monochromator was superior to mosaic crystal monochromators both in flux and resolution when optimal bending was used; the same is true for the analyser (Pattison *et al.*, 1986). Another spectrometer was built for operation with a rotating-anode generator (Lienert, 1995). With Mo $K\alpha_1$ radiation and a 0.7 mm-thick Si crystal sample the count rate averaged over the Compton profile was 65 counts s^{-1}, and the resolution was 0.16 a.u., *i.e.* the performance of the scanning-type laboratory spectrometer was close to that of some Cauchois-type spectrometers operating at synchrotron sources. The peak-to-background ratio was about 100:1, which is much better than that available with Cauchois-type spectrometers. Excellent long-term stability was achieved, and the overall performance of the spectrometer encouraged us to build a similar instrument for the High Energy Inelastic Scattering Beamline of the ESRF.

2. X-ray optics for bent crystals

The use of bent crystals in X-ray spectrometers was originally motivated by the Rowland circle geometry, where a large solid angle for the scattered beam could be combined with good energy resolution. However, it was realised that the integrated reflectivity of a perfect crystal increased towards the kinematical limit when the crystal was bent (White, 1950). This enhancement could not be fully utilized in actual spectrometer constructions before large perfect crystals of Si and Ge became available. Construction of optimized spectrometers for conventional X-ray sources required the development of models for bent crystals where the geometrical conditions were combined with the results of dynamical diffraction theory. Computer codes were written for calculating reflectivity curves for bent crystals, and the results of these calculations were verified in several experiments (Erola *et al.*, 1990; Schulze & Chapman, 1995; Schulze *et al.*, 1994). At the moment, the calculation of reflectivity curves of bent perfect crystals can be considered as a well established routine, and the results can be used with confidence for optimization of actual constructions.

Another aspect of spectrometer construction is understanding the radiation source, monochromator, sample, analyser and detector to compose an integral X-ray optical system. For the best performance, all the components must match, and in the following the salient results for reflectivities of bent crystals and diffraction geometry are summarized briefly.

2.1. *Focusing by a bent crystal*

Fig. 1 shows equatorial focusing by a cylindrically bent Bragg crystal. The bending radius ρ is the diameter of the focusing (Rowland) circle. In the general case, the source and the focus are not on the Rowland circle, and the focal distances satisfy the following equation (Suortti *et al.*, 1994),

$$p_0/p + q_0/q = 2, \tag{1}$$

where

$$p_0 = \rho \sin(\theta_0 + \alpha), \tag{2}$$

$$q_0 = \rho \sin(\theta_0 - \alpha). \tag{3}$$

Here θ_0 is the Bragg angle for the central ray, and α is the angle between the Bragg planes and the crystal surface. In the figure, $\alpha > 0$, so that $p_0 > q_0$, and the sign conventions are such that p, q and ρ are all positive in the present case. The chord between the source and focus is

$$s = (p^2 + q^2 + 2pq\cos 2\theta)^{1/2}. \tag{4}$$

The monochromator and analyser crystals are of the Johann type in the present case, so that the surface of the

crystal does not coincide with the focusing circle. The Johann aberration increases the angle of incidence of a divergent ray from that for the central ray. A relation between the angles can be inferred from Fig. 1,

$$\rho[\cos(\theta+\alpha)-\cos(\theta_0+\alpha+\varphi)]=p_0\sin\varphi, \qquad (5)$$

where θ is the angle of incidence for a ray that makes an angle φ with the central ray. In the second-order approximation,

$$\delta\theta_J=\theta-\theta_0=(1/2)\cot(\theta_0+\alpha)\varphi^2. \qquad (6)$$

When the source is not on the Rowland circle the angle of incidence varies along the crystal, and a band of energies is reflected,

$$\begin{aligned}\Delta E/E&=\cot\theta\,(\varphi_2-\varphi_1)(p_0/p-1)\\&=(1/2)\cot\theta\,(\varphi_2-\varphi_1)(p_0/p-q_0/q),\end{aligned} \qquad (7)$$

where $\varphi_2-\varphi_1$ is the angular width of the incident beam. There is an energy gradient in the reflected beam, as indicated in Fig. 1, and it is important that the direction of the gradient is reversed when the geometrical focus is crossed.

2.2. *Reflectivities of bent crystals*

The angular width of a reflection from a perfect crystal is inversely proportional to the extinction length Λ_S, and for a thick crystal the width of the total reflection in the Bragg case or the FWHM in the Laue case is the Darwin width,

$$\delta\theta_D=(4r_e d^2/\pi V_c)kF'\tan\theta=2\lambda/\pi\Lambda_S\sin 2\theta, \qquad (8)$$

where d is the spacing of Bragg planes, $r_e=e^2/mc^2=2.82\times10^{-5}$ Å is the electron scattering length, V_c is the volume of the unit cell, λ is the X-ray wavelength, k is the polarization factor (1 for the σ component perpendicular to the scattering plane, and $\cos 2\theta$ for the π component scattered through angle 2θ) and F' is the real part of the scattering factor. In the case of an asymmetrical reflection, the width of the reflection is the Darwin width multiplied by $M^{1/2}$, where M is the lateral magnification of the beam upon reflection. The relative energy band reflected by the crystal is

$$(\Delta E/E)_D=\cot\theta\,\delta\theta_D, \qquad (9)$$

which is independent of energy as far as k and F' are constant.

The Darwin width in the energy scale is 10^{-4} for the lowest-order reflections of Si and Ge, and decreases rapidly for higher-order reflections, as seen from (8). This situation is changed profoundly when the crystal is bent in the plane of diffraction. The incident wave propagates in a crystal where the lattice phase changes continuously, and the interaction distance is limited by the curvature of the crystal. Roughly speaking, when the orientation of the Bragg planes changes by the Darwin width of the reflection over the extinction length, the crystal begins to behave like an imperfect crystal obeying kinematical diffraction theory. A good description of the situation in the Bragg case is given by the lamellar crystal model where each lamella is a perfect crystal but where the orientation and lattice spacing of the lamella changes according to the curvature of the crystal (Boeuf *et al.*, 1978).

The change of the energy reflected over the thickness T in a bent crystal is due to the change of the orientation of the Bragg planes and to the change in lattice spacing (Suortti & Thomlinson, 1988; Erola *et al.*, 1990). If elastic anisotropy is ignored and the lamellar model is used, the relative energy change is

$$\begin{aligned}\delta E/E&=-\cot\theta\,(T/\rho)\{\tan(\chi+\theta)+(1/2)(1+\nu)\sin 2\chi\\&\quad-\tan\theta[\cos^2\chi-\nu\sin^2\chi]\}\\&=-\cot\theta\,(T/\rho)[\cos(\chi+\theta)B(\theta,\chi)]^{-1},\end{aligned} \qquad (10)$$

where $\chi=\pi/2-\alpha$ is the angle between the surface normal of the crystal and the Bragg planes ($\pi/2$ for symmetrical Bragg reflection, 0 for symmetrical Laue reflection), and ν is the Poisson ratio. The signs are chosen such that ρ is positive when the beam enters on the concave side, and $\chi+\theta$ is the angle between the beam and the surface normal.

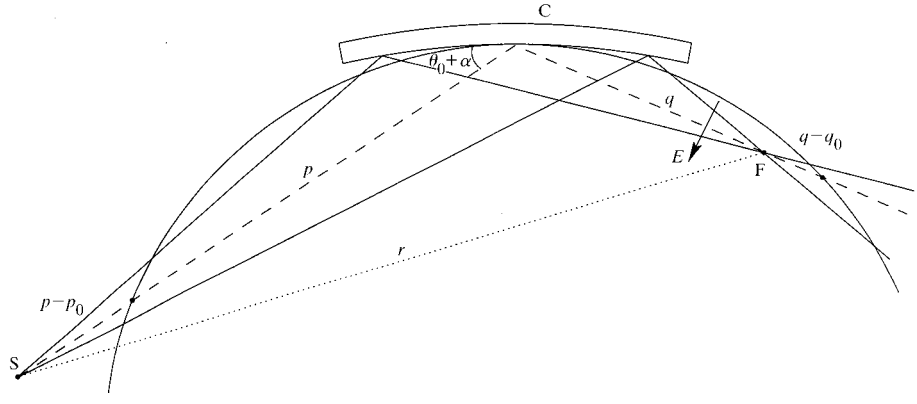

Figure 1
Rowland circle geometry for a bent Johann-type crystal C. The bending radius of the crystal is the diameter of the circle, θ_0 is the Bragg angle, and α is the asymmetric cut angle. In the figure, the source S is outside the focusing circle and the focus F is inside. This introduces an energy gradient, which is indicated by an arrow.

When a pencil beam traverses the thickness T, an energy band given by (10) is reflected, but the change of the Bragg angle is given by

$$\delta\theta = (T/\rho)[\tan(\chi + \theta) + \sin\chi(\cos\chi + \nu\sin\chi)], \qquad (11)$$

where the first term, which arises from the curvature of the crystal, is dominant when χ is large, as in the present case. Accordingly, there is a correlation between the direction and energy of the diffracted beam, which is important for understanding the focusing properties. A polychromatic focus forms at distance L (Suortti *et al.*, 1994),

$$L = \rho\sin 2\theta/2\sin(\chi + \theta), \qquad (12)$$

and, at the geometrical focus given by (1), the width of the beam due to polychromatic focusing is

$$\Delta x = T[\sin 2\theta/\cos(\chi + \theta)](|q - L|/L). \qquad (13)$$

In the Bragg geometry, the geometrical and polychromatic focii coincide only in the case of symmetrical reflection. The energy gradient arising from the active thickness of the bent crystal is to be combined with the gradient given by (7). It is possible to have a suitable energy gradient across the sample volume, and this can be utilized in dispersion compensation by the analyser crystal, as discussed later.

The reflectivity curve for radiation of a given energy is calculated in the lamellar model by correlating the Bragg angle inside the crystal with the absorption path length. The reflectivity curve has a sharp edge at the low angle side, corresponding to the crystal surface, with an exponential decrease towards higher angles. An approximate functional form is obtained from (10),

$$R(\varepsilon) = \exp(-a\mu\rho B\varepsilon), \qquad (14)$$

where $a\mu = [1 + \sin(\theta + \alpha)/\sin(\theta - \alpha)]\mu$ is the linear absorption coefficient in asymmetrical Bragg diffraction, and $\varepsilon = \theta(T) - \theta(0)$. More precise results may be obtained from computer codes based on the lamellar crystal model, where the reflectivity curves for different states of beam polarization are calculated separately (Eteläniemi *et al.*, 1989).

The energy band reflected by a bent crystal may be much larger than the band corresponding to the Darwin width of the reflection. The enhancement factor e of intensity is the integrated reflectivity of the bent crystal divided by the integrated dynamical reflectivity; when the effects of absorption are ignored,

$$e = R(\delta E/E)/[(4/3)\cot\theta\,\delta\theta_{\rm D}], \qquad (15)$$

where R is the average reflectivity of the bent crystal. A rough estimate for e is obtained by comparing the effective crystal thicknesses of bent and flat crystals, *i.e.* T *versus* $\Lambda\cos(\chi + \theta)$. The maximum value of e is the ratio of the integrated reflectivity of the ideally imperfect crystal to that of the perfect crystal. It has been demonstrated that this limit is achieved when the bending radius of the crystal is decreased (Erola *et al.*, 1990; Schulze & Chapman, 1995). The enhancement is spectacular at high energies where the active crystal thickness is not limited by absorption, so that e may be of the order of 100 (Suortti *et al.*, 1992).

3. Synchrotron radiation source and monochromator

The High Energy Inelastic Scattering Beamline (BL25 or ID15B) is located at the insertion device port 15 at the ESRF. There are two different insertion devices, which serve three separate experimental stations. The asymmetrical multipole permanent-magnet wiggler (AMPW) has seven periods and a maximum critical energy of 45 keV at 1.86 T magnetic field. The width of the radiation fan is ± 2.2 mrad. The superconducting wavelength shifter (SCWS) has a centre pole, where the maximum field is 4 T (critical energy 96 keV), and compensating side poles of about one-third of the field. The radiation fan extends from -6 mrad to $+6$ mrad. Both insertion devices provide circularly polarized radiation above and below the orbit plane. A beam splitter is located immediately after the shield wall at 27 m from the source, and the openings are 1.2 mrad for the central beam, 0.8 mrad to the starboard side and 1.0 mrad to the port side. The separations between the beams are 1.0 mrad. In the operation with the AMPW only the central beam is used, and two successive and semi-transparent monochromators for the port and starboard side stations can be inserted, still leaving an attenuated white beam for the central (bow) station. In the operation with the SCWS the respective side beams are reflected to the port and starboard stations, so that all three stations can be operated fully independently.

BL25 is on the starboard side, and it is served by horizontally focusing Johann-type monochromators, which are placed at 42 m from the centre of the AMPW and 40 m from the SCWS. The scattering angle is 7.5°, and the crystals have the value $\alpha = 2.5°$ for 5:1 demagnification (or $\alpha = 2.3°$ for 4.2:1 ratio). The length of the AMPW is 1.6 m, so it can be calculated from (7) that an energy band $\Delta E/E = 4.6 \times 10^{-4}$ is reflected from an incident radiation fan of 0.8 mrad. However, the distribution of incident angles on the monochromator corresponds to a much narrower relative energy band ($<10^{-4}$). The monochromator is built on a stage of longitudinal and transverse translations, horizontal rotation, and transverse and longitudinal tilts. These allow fine adjustment and energy tunability of 15%. Low-order reflections of Si are used, and the parameters are collected in Table 1. The crystals are 400 mm long, the upper and lower edges are 5 mm thick while the 10 mm-high middle part is only 1 mm thick. There are three crystals placed above each other for an easy change of energy, and the cooling frames have a horizontal slot in the middle for the direct beam to be transmitted to the central station.

The most critical part of the whole experimental station has turned out to be the monochromator, which focuses the beam onto the sample. Different designs have been studied and extensive tests have been carried out. The basic idea of the construction is that the power loading along the crystal

Table 1
Si monochromators used at beamline ID15B.

The 400 mm-long crystals are bent cylindrically to a radius of 385 m, the Bragg angle is 3.75°, the asymmetric cut 2.5° (2.3°) for 5:1 (4.2:1) demagnification, and the thickness 1 mm. E_0 is the incident energy and P is the integrated reflectivity. The calculated flux F_c is the spectral flux from the asymmetric multipole wiggler (AMPW) or from the superconducting wavelength shifter (SCWS), as attenuated by beamline filters and Be windows, multiplied by the integrated reflectivity of the monochromator in energy scale. The measured flux F_m is that through a 0.2 mm-wide and 6 mm-high slit at the focus. The values have been normalized to 100 mA of the storage ring current.

hkl	E_0 (keV)	P (μrad)	F_c (counts s^{-1}) (AMPW)	F_m (counts s^{-1}) (AMPW)	F_c (counts s^{-1}) (SCWS)
111	30.6	5.77	12.5	3.5	1.1×10^{11}
220	49.0	7.70	27.6	4.5	3.8
311	58.0	7.15	24.9	7.8	4.1

is uniform. Thermal contact for cooling is by the upper and lower edges of the crystal, so that the heat flow is perpendicular to the footprint of the beam. In the ideal case there is only a vertical temperature distribution, which is symmetrical about the centreline of the crystal, and this does not distort the cylindrical shape, which is effected by equal moments acting at the ends of the crystal. A temperature gradient of 1 K mm^{-1} perpendicular to the crystal surface curves a free crystal to a radius of 300 m. The nominal bending radius of the Bragg monochromators is 385 m, so that cooling should eliminate the thermal gradient or the thermal effects are compensated by a suitable bending mechanism. This is not a trivial task, as about 5 W cm^{-1} is absorbed in the crystal, and the deviations from the cylindrical shape should be kept smaller than 10 μrad.

A detailed report on the bending and cooling mechanism of the Bragg-type monochromators will be published separately, and only the principle is shown in Fig. 2. The thermal contact of the thick edges of a crystal to the water-cooled frame is made by pockets of InGa eutectic. The crystal is clamped at one end and bent to a cylindrical shape by a perpendicular leaf spring that produces a moment at the free end. A spring of suitable stiffness compensates for a thermal curving of the crystal. It is important that the displacement of the tip of the spring is much larger than movements due to thermal drifts of the support structures.

The monochromatic beam was characterized by scanning a narrow horizontal slit across the beam and by analysing the energy distribution by a vertically diffracting perfect crystal. The beam is focused at the collimating slit located 8.1 m from the monochromator, and a beam width of less than 0.4 mm has been achieved, as shown in Fig. 3. The bending radius is obtained from (1), (2) and (3), yielding ρ = 378 m. The corresponding values for the distances to the Rowland circle are p_0 = 41.20 m and q_0 = 8.25 m; *i.e.* the crystal is slightly overbent, which is the case shown in Fig. 1. The energy band from (7) is $\Delta E/E = 2.4 \times 10^{-4}$. The distance of the polychromatic focus, as calculated from (12), is 24.5 m, and the total bandwidth from a 1 mm-thick crystal is $\delta E/E = 3.7 \times 10^{-4}$. The two gradients are in opposite directions downstream from the focus, so that a partial cancellation is expected. The observed energy band of 60 keV radiation is about 20 eV. The width of the focus, as calculated from (13), is 0.8 mm, which is more than that observed, but this is expected because the FWHM of the reflectivity curve is given by (14) rather than (11).

The photon flux of the incident beam was determined by measuring Compton scattering from Al and Si samples of known thicknesses. The flux scattered to the solid angle Ω is

$$n_c = n_0 \Omega (\mathrm{d}\sigma/\mathrm{d}\Omega)_c (1 - A) t, \qquad (16)$$

where n_0 is the incident flux, $(\mathrm{d}\sigma/\mathrm{d}\Omega)_c$ is the scattering cross section per unit length of the sample, t is the effective sample thickness in the direction of the beam, and $(1 - A)$ is the transmission factor. The scattering cross section for one electron can be calculated from the Klein–Nishina formula, so that

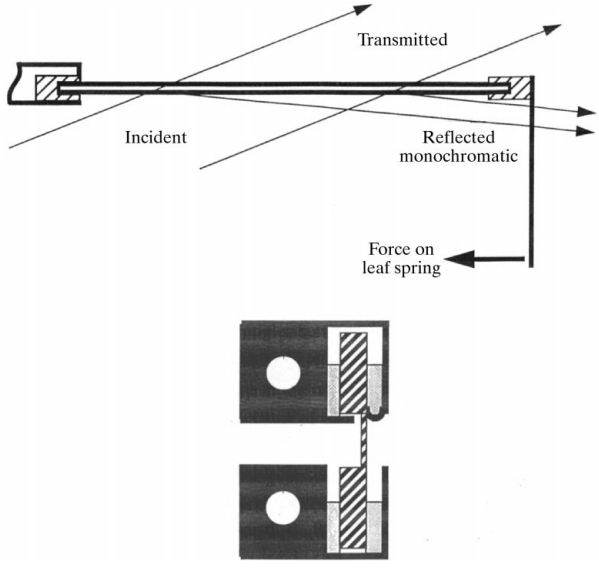

Figure 2
Monochromator construction showing the principle of bending and cooling. The crystal is clamped at one end and bent to cylindrical shape by a moment acting on the free end *via* a leaf spring. The incident beam is reflected and partly transmitted by the thin centre part of the crystal. The cross section of the crystal (hatched) and the cooling frame are shown in the lower figure. Cooling is achieved by pockets of InGa, which are in direct contact with the crystal and the water-cooled copper frame.

$$(d\sigma/d\Omega)_c = M_0(d\sigma/d\Omega)_{K-N}$$
$$= M_0(1/2)r_e^2(E/E_0)^2\{[E/E_0 + E_0/E] - (1 - P_1)\sin^2\Theta\}, \quad (17)$$

where M_0 is the number of electrons per unit volume, E_0 is the energy of the incident photon, E is that of the scattered photon, P_1 is the degree of linear polarization in the plane of scattering (close to -1 in the present case), and Θ is the scattering angle.

The calculated performance of the monochromators is summarized in Table 1. Normally the reflections with odd indices are used to avoid the effects of the first harmonic reflection, and these provide a flux of 10^{12} photons s^{-1} between 30 keV and 100 keV when the AMPW is used. The measured values for the three lowest energies correspond to the flux through a 0.2 mm-wide slit, which passes typically about 30% of the beam. The experimental results show good agreement with calculation.

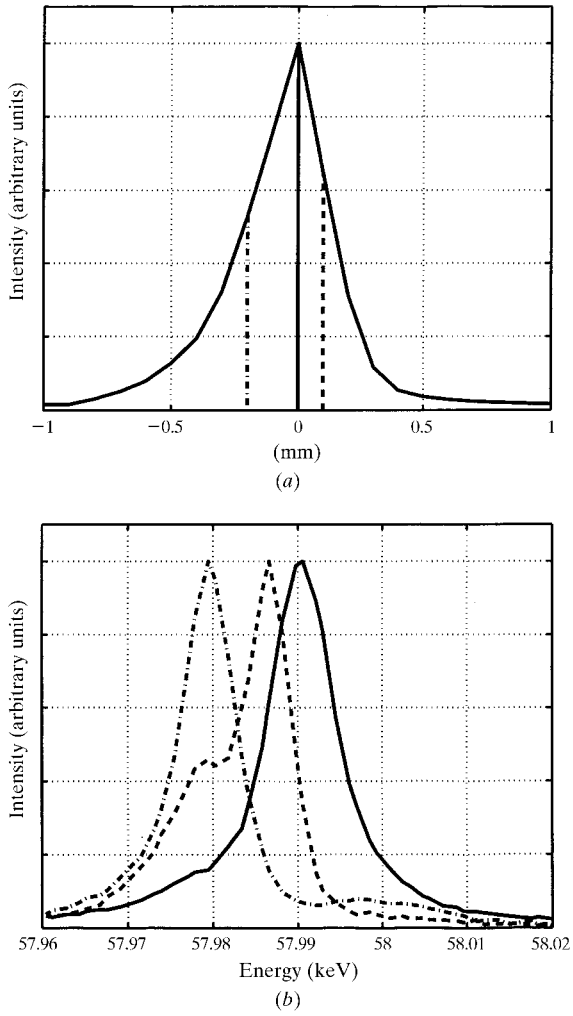

Figure 3
Beam size (*a*) and spectral distribution (*b*) of the monochromatic 58 keV beam at the focus. The beam was scanned with a 0.05 mm slit (*a*). The FWHM was 0.35 mm when the storage ring current was 80 mA, and this increases to about 0.5 mm when the current is 200 mA. The energy distribution was analysed by a vertically reflecting perfect crystal at three locations of the focused beam. The FWHM at a given point is 7.5–9.0 eV, and the total span of energies in a 0.3 mm-wide beam is 29 eV.

4. Scanning spectrometer

The present spectrometer has been built to operate in the mode where the scattered spectrum is recorded sequentially by rotating the analyser crystal and maintaining the focusing geometry by synchronized rotations and translations of the analyser and detector. However, the construction allows dispersing of the spectrum in space by the analyser crystal and use of a position-sensitive detector. The use of the scanning mode is made possible by the high degree of stability of the synchrotron source, and it offers several advantages over the energy-dispersive mode, most notably low background and selective recording of the interesting parts of the scattered spectrum.

The construction of the spectrometer is shown in Fig. 4. The sample is placed on a separate stage, and the analyser crystal and the detector with their translation and rotation stages are placed on a large table. The scattering angle can be varied from 0 to 173° by rotating the table about a pivot placed below the sample. The sample stage can carry large cryostats or magnets. The sample chamber can be translated longitudinally and transversely, lifted, and rotated or tilted about three orthogonal axes. The incident beam is collimated by a horizontal slit and limited vertically depending on the sample size, or a circularly polarized beam can be extracted for magnetic scattering studies.

The first intensity monitor is an Si diode placed in the incident beam after the collimating slit, and scattering from the sample is monitored with a Ge detector. As the size of the incident beam on the sample is usually less than 0.5 mm horizontally and 5 mm vertically, small samples can be studied.

4.1. *Spectrometer geometry*

The radius of the Rowland circle and the scattering angle 2θ are constant in the present spectrometer. Equations (1)–(4) apply, and positioning and motions of the stages are shown in Fig. 4 using coordinates that refer to the spectrometer table. When the sample and receiving slit are on the Rowland circle,

$$X = \rho_a \sin 2\theta_a \cos(\theta_a - \alpha - \gamma_0), \quad (18)$$

$$Y = \rho_a \sin 2\theta_a \sin(\theta_a - \alpha - \gamma_0), \quad (19)$$

$$\beta = 2\theta_a - \gamma_0, \quad (20)$$

where ρ_a is the bending radius of the analyser crystal of an asymmetric-cut angle α and Bragg angle θ_a, β is the rotation angle of the detector, and γ_0 is the angle between the analyser and detector translations.

In the general case the sample and the receiving slit may not be on the Rowland circle, so that

$$X = s\cos(\gamma - \gamma_0), \quad (21)$$

$$Y = s\sin(\gamma - \gamma_0), \tag{22}$$

where

$$\tan\gamma = q\sin 2\theta_a/(p + q\cos 2\theta_a), \tag{23}$$

and the distance s between the sample and receiving slit is given by (4). An explicit relation between the focal distances, asymmetric cut and bending radius is obtained from (1)–(4),

$$2pq = \rho[p\sin(\theta_a - \alpha) + q\sin(\theta_a + \alpha)]. \tag{24}$$

The zero angle of the analyser crystal can be measured optically or mechanically, and ρ_a, α and the optimal sample and receiving-slit positions can be determined by recording several fluorescence lines and elastic lines plus Compton peaks from suitable samples. However, it is advisable to measure ρ_a and α using a laboratory X-ray source before installation of the analyser.

4.2. *Resolution function*

The energy resolution of the spectrometer arises from several factors: distribution of energy in the beam incident on the sample, effective volume of the sample, divergences of the beam reflected by the analyser, and the reflectivity of the analyser. There is a correlation between the incident energy, location of the scattering element, and the energy reflected by the analyser, so that a straightforward convolution of the individual functions is not justified in the general case. There is a possibility for dispersion compensation, and position–angle correlations also have implications on the calculation of multiple scattering. The sample geometry is shown in Fig. 5, and it is seen that there is a shift in reflected energy,

$$\delta E = E\cot\theta_a(x'/p) = -E\cot\theta_a\delta\theta_a(x'), \tag{25}$$

when the scattering volume element is off the centreline of the scattered beam. The shift can be compensated by a gradient of energy across the beam, and this can be regulated by the position of the geometrical focus, as already discussed in §3. It was noted that the gradients due to polychromatic and geometrical focusing add up, and in the present case the first one makes the energy increase inwards (towards the centre of the focusing circle) while the second gradient is inwards before the geometrical focus and outwards after the focus. The direction of the gradient, as seen by the analyser, depends also on the sample geometry. If the sample is a disc, dispersion compensation is achieved when the energy gradient is outwards in reflection geometry and inwards in transmission geometry. The use of dispersion compensation requires high stability of the monochromatic beam, and so far it has not been utilized. In the following discussion the incident beam is assumed to have a uniform narrow distribution of energies.

In the general case, the dimensions of the sample give the boundary conditions for the integration limits of the incident and scattered beams, so that sample shape and absorption can be used for optimization of the resolution function. The general form of the resolution function due to the active sample volume is

$$g(x') = \int g(x, z)\exp[-\mu_0\Delta y - \mu\Delta y']\,\mathrm{d}y'\mathrm{d}z, \tag{26}$$

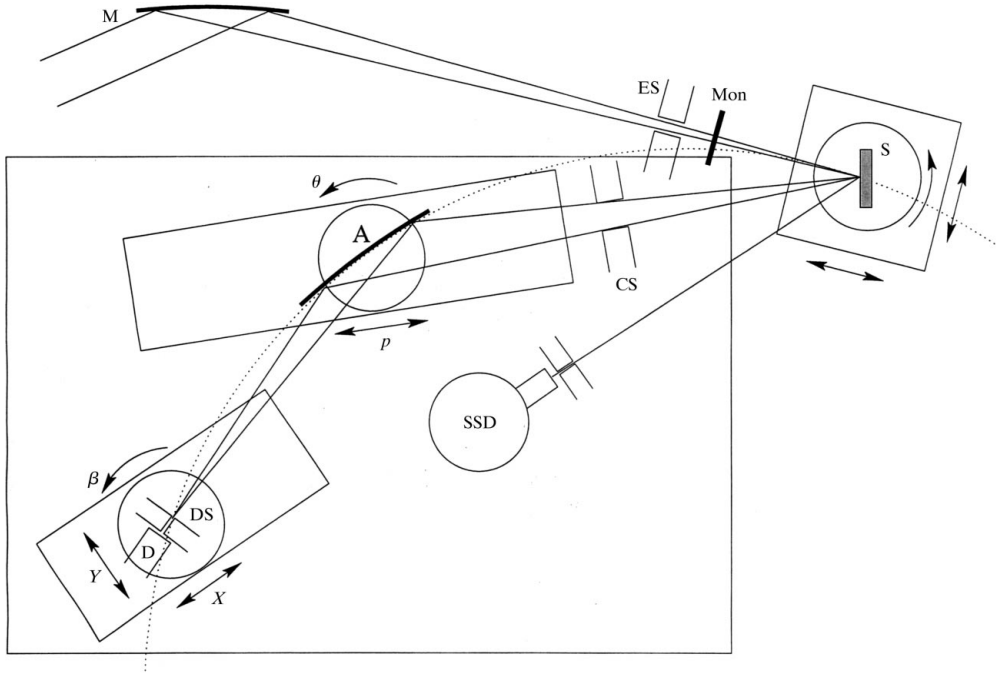

Figure 4
Geometry of the scanning spectrometer. The beam is focused on the sample S by the monochromator M and collimated by the entrance slit ES, which is followed by an incident beam monitor Mon. The sample is located in a vacuum chamber on top of a stage, which provides translations and rotations. The bent analyser crystal A moves along the scattering direction and rotates during the scan. The detector slit tracts the focus of the analyser crystal by translations X, Y and rotation β. Scattering is monitored by a Ge detector SSD.

where $g(x, z)$ is the intensity distribution of the incident beam, μ_0 is the absorption coefficient for incident radiation, μ is that for scattered radiation, and Δy and $\Delta y'$ are the path lengths from the entry and exit points to the scattering volume element, respectively. An explicit form is obtained when the sample is a disc of thickness t and $g(x, z)$ is narrow. In the angular scale,

$$g(\theta_a) = \exp\{p(\theta_{a,0})(\theta_a - \theta_{a,0})/\sin 2\theta_{a,0}[\mu_0 + \mu(\sin\eta/\sin\kappa)]\}, \quad (27)$$

with

$$\theta_{a,0} - [t/p(\theta_{a,0})](\sin 2\theta_{a,0}/\sin\eta) < \theta_a < \theta_{a,0},$$

where $p(\theta_{a,0})$ is the distance of the centre of the analyser from that of the sample, $\theta_{a,0}$ is the corresponding reflection angle, and η and κ are the angles between the sample surface and the incident and scattered beams, respectively. When η or κ are small, the corresponding path length is limited by the size of the disc, and $g(\theta_a)$ is modified accordingly.

The horizontal intensity distribution $g(x)$ of the incident beam is measured during the alignment procedure. The distribution is cut by a slit of width w_x, so that the angular range of the distribution, as seen from the analyser crystal, is limited accordingly,

$$\theta_{a,0} - [w_x/2p(\theta_{a,0})](\sin\kappa/\sin\eta) < \theta_a < \theta_{a,0} + [w_x/2p(\theta_{a,0})](\sin\kappa/\sin\eta). \quad (28)$$

The combined effect of absorption in a disc-shaped sample and the intensity distribution of the incident beam is obtained by convoluting $g(\theta_a)$ from (27) by $g(x)$ within the angular limits given by (28). Model calculations can be used for optimization of resolution and scattered flux, as demonstrated in performance tests.

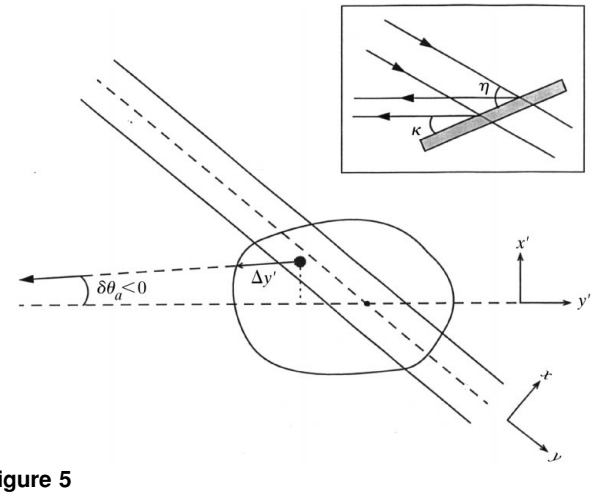

Figure 5
Beam paths in a horizontal cross section of a sample of convex shape. The coordinate y is along the centreline of the incident beam, x is perpendicular to y in the scattering plane, y' and x' are the corresponding coordinates with respect to the scattered beam. In the general case the cross section depends on the axial coordinate z, and an integration is needed. In the insert a disc-like sample in the asymmetric reflection geometry is shown.

The analyser crystal is bent cylindrically to a radius equal to the diameter of the focusing circle. This introduces a deviation from ideal focusing, namely the Johann error, which has already been mentioned. There is an increase of reflection angle, which is obtained from (6). The axial (vertical) divergence ψ decreases the reflection angle approximately by

$$\delta\theta_{a,v} = -(1/2)\psi^2 \tan\theta_a. \quad (29)$$

Cumulative distributions are used for the geometrical contributions to the resolution function in order to avoid the effects of singularities. The distribution function due to the Johann error is

$$G_J(\theta_a) = 1 - (1/\varphi_m)\arccos[\cos(\theta_a + \alpha)/\cos(\theta_{a,0} + \alpha)], \quad (30)$$

with

$$\cos(\theta_{a,0} + \alpha)\cos\varphi_m < \cos(\theta_a + \alpha) < \cos(\theta_{a,0} + \alpha),$$

where φ_m is the maximum equatorial divergence of the scattered beam. The distribution function due to the axial divergence is

$$G_A(\theta_a) = 1 - [\sin^2\theta_{a,0} - \sin^2\theta_a]^{1/2}/\psi_m \sin\theta_{a,0}, \quad (31)$$

with

$$\sin^2\theta_{a,0}(1 - \psi_m^2) < \sin^2\theta_a < \sin^2\theta_{a,0},$$

where ψ_m is the maximum axial divergence of the scattered beam.

The resolution function is measured by scanning spectra of elastically scattered radiation and narrow fluorescence lines from suitable samples. There are two important differences, however. First, the fluorescence lines are Lorentzians of known natural widths and, second, the active thickness of a fluorescent sample is small. For an experimental resolution function, the fluorescent spectra must be convoluted by the energy band of the incident beam and the function $g(x')$ from (26), while the broadening due to the natural widths of the fluorescence lines must be subtracted.

When a fixed energy is scanned by the spectrometer, the recorded intensity distribution is $I(-\delta\theta_a)$, which is converted to $I(\delta E_c)$ through

$$(\partial\theta/\partial E) = -\tan\theta_a/E; \quad (32)$$

i.e. the measured resolution function has, in the energy scale, the same symmetry as the resolution function calculated by successive convolutions of the geometrical aberrations in the angle scale. The effect of the reflectivity curve of the analyser is similar; when a fixed energy is scanned, the active layer of the crystal moves from inside of the crystal to the surface when the angle is increased, while, at a given angle, inner parts of the crystal reflect lower energies from a polychromatic beam. This is included explicitly in (32), and the approximate form of the reflectivity curve is given by (14).

The resolution function of the scanning spectrometer under typical conditions is shown in Fig. 6, where the calculated functions are shown together with the measured elastic line profile. The perfect agreement demonstrates that the resolution of the spectrometer is well understood and can be calculated and optimized using the model functions given above.

4.3. *Response function*

The response of the spectrometer as a function of energy is obtained by integrating over the resolution functions given above. In addition, changes in the scattering cross section and the beam transmission between the sample and detector, $(1 - A)$, must be included. The present spectrometer operates in air, and attenuation increases with decreasing energy because of the increase of the absorption coefficient and the absorption path length $2\rho \sin\theta_a \cos\alpha$. The solid angle Ω subtended by the analyser and the receiving slit may change during the scan. There is a fixed horizontal slit between the sample and the analyser, and therefore the same length of the analyser crystal is effective during the scan. On the other hand, the axial opening angle may be defined by a fixed slit, the height of the analyser crystal or by that of the receiving slit. The response of the detector is discussed in the following section.

For practical reasons, the scattered spectrum is recorded as a function of the analyser rotation angle. Conversion between the angle and photon energy is given by (32). The energy spectrum of Compton scattering is converted to the momentum scale through the relation

$$p_z = mc[r - 1 - E(1 - \cos 2\theta)/mc^2]/(1 + r^2 - 2r\cos\Theta)^{1/2}, \quad (33)$$

where m is the electron rest mass, c is the velocity of light and $r = E/E_0$. In atomic units, $mc = 137$.

4.4. *Performance tests*

It was already mentioned in §3 that the actual performance of the monochromator is close to predictions, so that typically about 10^{12} photons s^{-1} of an energy band of 20 eV pass through a collimating slit of width 0.2 mm and height 6 mm.

The efficiency of the spectrometer is proportional to Ω, $(1 - A)$, the integrated reflectivity P_a of the analyser crystal, the efficiency e_D of the detector, and the effective thickness $t_{\rm eff}$ of the sample (Suortti *et al.*, 1986*b*). The average count rate within a scan range $\Delta\theta_a$ from θ_{a1} to θ_{a2} is

$$n_c = n_0(\Omega/\Delta\theta_a)P_a(\mathrm{d}\sigma/\mathrm{d}\Omega)_c e_D(1 - A)t_{\rm eff}. \quad (34)$$

Typical values are collected in Table 2, and they demonstrate that the response of the analyser is well understood and close to the theoretical limit. The 25% loss of intensity with 56 keV radiation is presumably due to non-ideal bending of the Ge(440) analyser crystal, which decreases the effective equatorial opening angle. The values are given for the nominal beam current of 100 mA although, under ideal conditions, 200 mA is a more typical value.

The equatorial focusing condition of the analyser crystal is fulfilled only for one set of reflections, for example, 2*h*,2*h*,0, and ideally only beams scattered by these reflections pass through the receiving slit. However, when the axial divergence of the beam is increased, reflections from

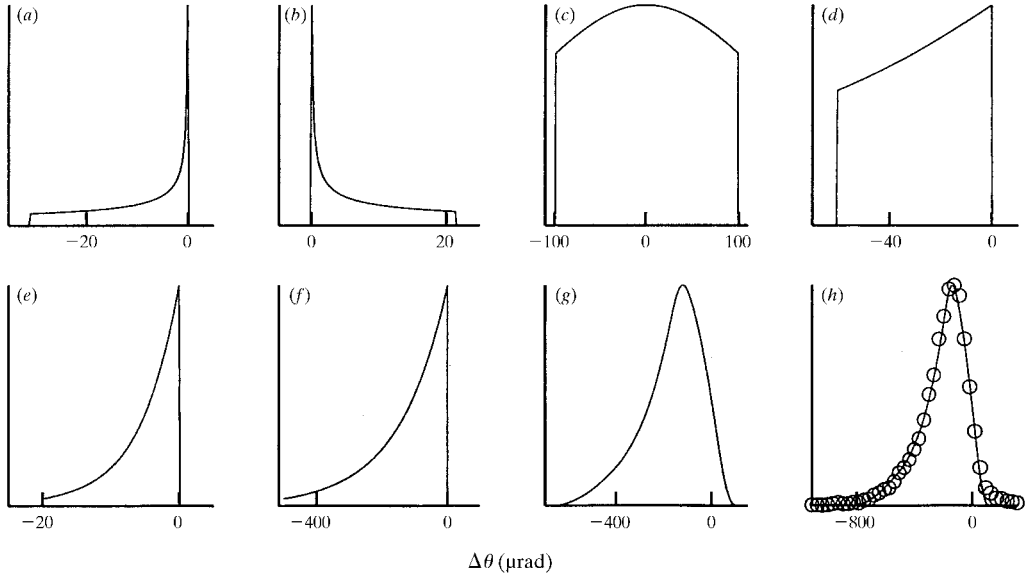

Figure 6
Components of the resolution function in the scattering plane. These include the Johann error (*a*), the effect of the axial divergences of the scattered beam (*b*), the intensity distribution of the 31.77 keV incident beam, as limited by a 0.3 mm slit (*c*), absorption in a disc-like 0.75 mm-thick Si sample in symmetrical reflection geometry (*d*), energy band of the incident beam from an Si(111) monochromator (*e*), and the reflectivity of the Si(400) analyser crystal ($\rho = 7$ m, $\alpha = 3.17°$) (*f*). A convolution of these functions is shown in (*g*). The measured profile of the elastic line is given by circles in (*h*) together with the calculated curve.

Table 2
Calculated and measured count rates at the detector of the scanning spectrometer.

The average count rate n is calculated from equations (17) and (34) for the angular scan range $\Delta\theta_a$, which corresponds to electron momenta between −10 and +10 a.u. (or −8.5 and +8.5 a.u.), and n_{max} is the count rate at the Compton peak. The values have been normalized to 100 mA of the storage ring current.

Sample	E_0 (keV)	Θ (°)	P_a (μrad)	$(d\sigma/d\Omega)_c$ (cm^{-1})	t_{eff} (mm)	n_{calc} (counts s^{-1})	n_{exp} (counts s^{-1})	n_{max} (counts s^{-1})
Al_2O_3	55.98	160	28.0	0.0577	0.76	597	452	2600
Al_2O_3	29.26	173	95.7	0.0748	0.65	318	315	1700

other Bragg planes may be detected. This occurs when the projection of the normal of a plane coincides with the normal of the proper equatorial reflection. For instance, when the proper reflection is 440 and the axial direction is [001], reflections from (*hhl*) planes may enter the receiving slit giving rise to a spectrum which is shifted in the angle scale. An example is shown in Fig. 7(*a*), where the elastic line reflected from (551) planes appears at the high-angle side of the proper Compton profile, and the Compton profile due to 551 increases the background in the tail of the proper Compton profile. These reflections are off the equatorial plane, so that their intensity is reduced with a narrow receiving slit or an axial Soller slit, but these make operation of the spectrometer more delicate.

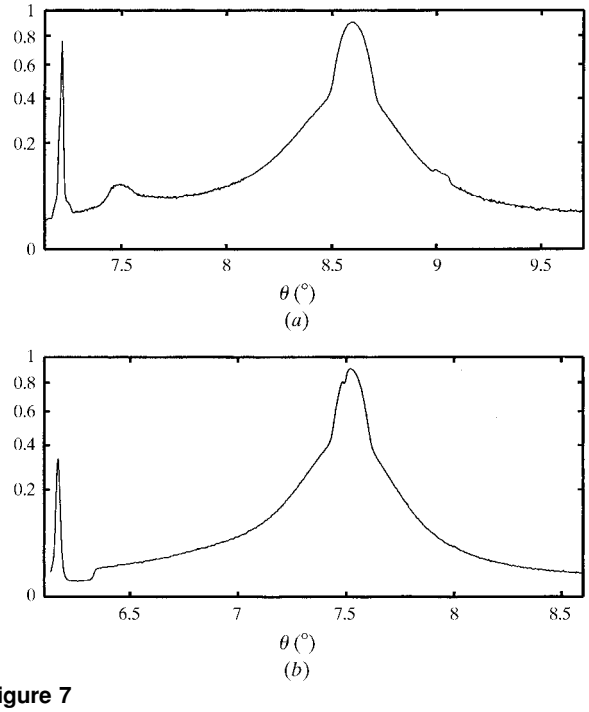

Figure 7
As-recorded spectra from a single-crystal Al sample using different monochromator and analyser crystals. The vertical scale is proportional to the square root of the intensity to emphasize the background. In (*a*), an Si(220) monochromator and Ge(440) analyser with [001] axis are used. The incident energy is 49 keV. Different parasitic contributions are identified, and they are discussed in §4.4. In (*b*), an Si(311) monochromator and Ge(440) analyser with [$\bar{1}$10] axis are used. The incident energy is 58 keV. The 'glitch' in the Compton profile at 7.494° is due to 'Aufhellung' by Ge(*hk*1) reflections.

At some energies of the spectrum being scanned the Bragg condition may be fulfilled for an off-equatorial reflection, which does not fall on the receiving slit. The effective absorption coefficient is increased by this reflection, and a local loss of intensity is seen in the spectrum, as shown in Fig. 7(*b*). In this case the proper reflection is again (4,4,0), the axial direction [1, $\bar{1}$, 0], and the asymmetry angle of the analyser is 2°. When the incident energy is 58 keV and the scattering angle is 160°, the Compton peak is at 47.6 keV. A family of reflections *hkl* is excited at θ_a = 7.494°, resulting in a 'glitch' near the Compton peak. Usually only a small part of the beam falling on the analyser crystal satisfies the condition for the extra reflection, so that the effect is small. The position of a glitch can be calculated, and it can be moved to a different place in the spectrum by changing the incident energy and/or scattering angle, but it may not be completely eliminated.

When there is more than one energy in the incident beam, like the harmonics arising from the 440 and 660 reflections of the Si(220) monochromator, corresponding parasitic spectra are scattered. For instance, the extra bump between the elastic line and Compton peak in Fig. 7(*a*) is due to Compton scattering of the 100 keV radiation, which is transmitted by the 660 reflection of the analyser. Fluorescent radiation from the sample may be reflected by off-equatorial planes or by the 220 reflection. In all of these cases the energy difference to the proper reflection is quite large, and most of the parasitic components can be rejected by an energy-dispersive detector. The strategy of processing the measured spectrum to yield the Compton profile is summarized in Fig. 8. The background is removed and the measured intensity is multiplied by a composite correction factor, which is the inverse of the response function discussed earlier. At each point of the spectrum the energy distribution is recorded by the scintillation detector and an MCA, and the parasitic components are resolved and subtracted from the total spectrum, as shown in the lower panels of Fig. 8. The basic idea of the background subtraction is to model the different components using theory or subsidiary measurements without resorting to such conditions as symmetry of the Compton profile or agreement with the theoretical free-atom profile at high momenta. These are necessary constrains but not sufficient for an overall determination of the background, and can be used only in the last stage where unspecified contributions to the background are being subtracted.

A particular contribution to the background is multiple scattering from the sample. A new Monte Carlo code was written for calculation of multiple scattering, and it was tested by measurements where multiple scattering was dominant. Polarization of photons is included throughout the calculation using Stokes parameters. The reflection at the analyser crystal is also included, and the width of the receiving slit limits the volume which contributes to the observed multiple scattering. The same condition applies to scattering from air in the vicinity of the sample (Fajardo *et al.*, 1998).

The background is mostly due to the parasitic components discussed above. Other scattering is eliminated by lead panels between the sample stage and the spectrometer, by local shielding of the detector and a beam tunnel between the analyser and the receiving slit. The background that does not originate from the sample is on the 1% level, and is recorded separately.

The Compton profile in Fig. 8 is almost perfectly symmetric. However, the resolution function changes slightly across the profile and, in order to compensate for this linear change, the final Compton profile $J(p_z)$ is taken as the average at positive and negative p_z. The count rate at the Compton peak may be as high as 5000 counts s^{-1}, and typically 400 points with 0.025 a.u. step size are recorded from +5 a.u. to −5 a.u.; for normalization, long scans from +15 a.u. to −15 a.u. are made. Accordingly, a statistical accuracy of 0.1% at the Compton peak is obtained in 1 d.

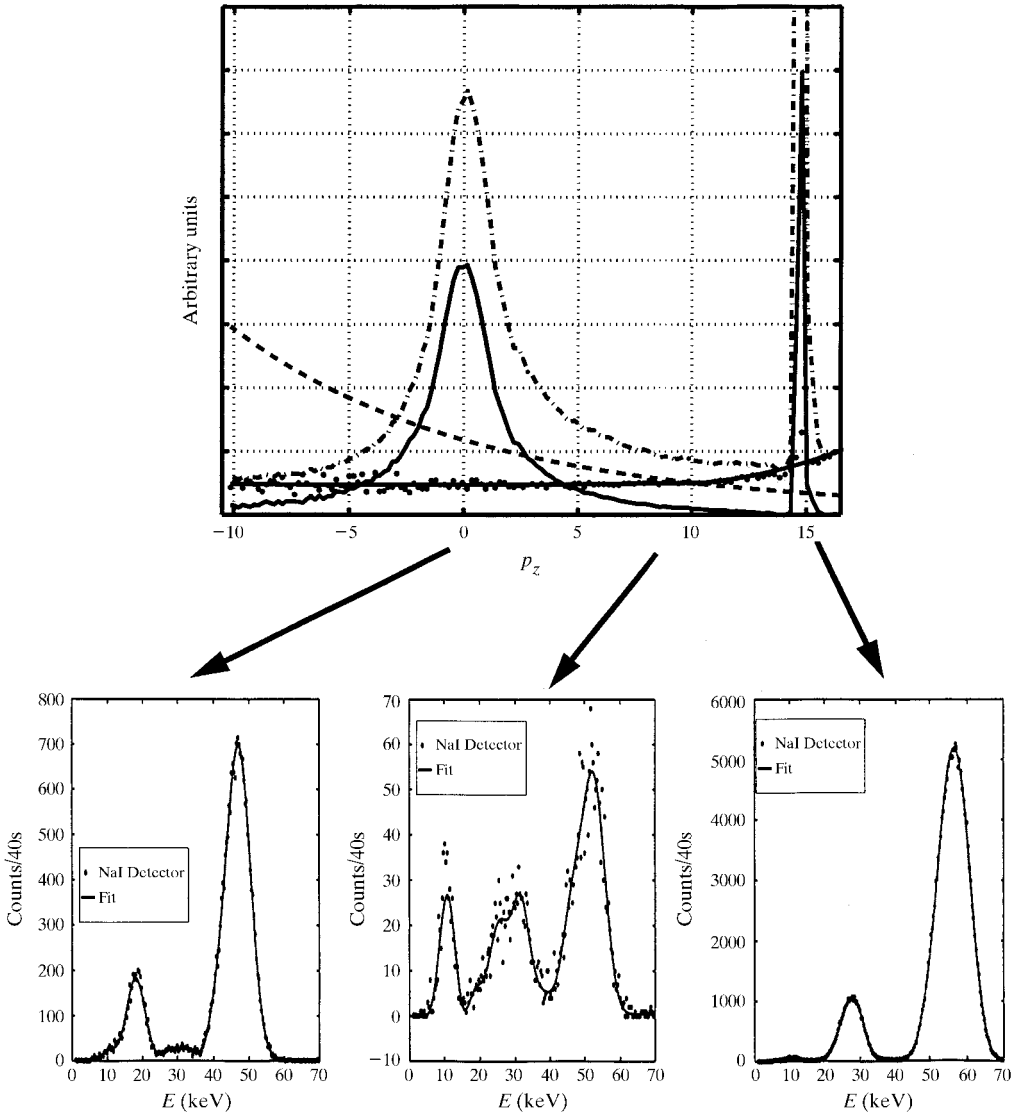

Figure 8
Processing the spectrum of scattered radiation. The sample is $YBa_2Cu_3O_7$ and the energy of the incident radiation is 57 keV. The upper panel shows the raw data (dash-dotted), the correction of the intensity due to changes in the response function and scattering cross section (broken line), the background with a fitted curve, and the final Compton profile (solid line). The analysis of the components of scattering are shown in the three lower panels. The components include the proper energy, for instance the elastic line in the panel to the right; the escape peak at about 30 keV lower energy due to iodine fluorescence in the detector; Ba, Y and Cu fluorescence entering the detector by air scattering; and Ge fluorescence from the analyser crystal. The solid line shows the fit of these components to the energy spectrum recorded by the NaI detector.

The results described above indicate that the absolute accuracy of the Compton profiles is on the same level, which allows detailed comparisons with the most sophisticated theoretical calculations.

5. Summary and conclusions

Compton scattering is an important method for studies of electronic states in solids. It probes the ground state of the system, when the conditions of the impulse approximation are met, so that it is one of the most direct methods for testing calculations of electron wavefunctions. The ever-increasing sophistication of these calculations puts higher and higher requirements on the experimental determination of Compton profiles. Only an optimized spectrometer operating at a third-generation synchrotron source can meet these requirements. The spectrometer described in this work was designed to provide Compton spectra of low and well understood background from small samples with good statistical accuracy and high resolution of the electron momenta. Therefore, a scanning spectrometer was constructed. The modular construction of the spectrometer allows for different sample environments, such as cryostats and magnets, and the scattering angle as well as the focal distances of the spectrometer can be changed according to the needs of the experiment. The special advantage of the scanning spectrometer is that only the interesting parts of the spectrum are recorded. The focusing geometry and narrow slit in front of the detector eliminate most effects of the extra reflections from the analyser crystal, and the remaining contributions can be estimated accurately.

The performance tests of the spectrometer show good agreement with the calculated flux at the detector and the energy resolution. The spectrometer is used routinely in the user experiments, and small details are continuously improved. The present energy range of the spectrometer is from 30 keV to 60 keV, which makes it difficult to study compounds with medium weight and heavy elements due to increased absorption. The energy range may be expanded beyond 100 keV if a Laue-type analyser crystal is used. The reflectivity of a bent crystal in Laue geometry is high, the band-pass can be optimized, and the geometrical aberrations are small, but the background is higher than in the Bragg geometry because of the larger opening of the detector. However, it should be possible to eliminate this problem by Soller slits in front of the detector, and these features are implemented in the new version of the spectrometer under construction.

References

Berthold, A., Mourikis, S., Schmitz, J. R., Schülke, W. & Schulte-Schrepping, H. (1992). *Nucl. Instrum. Methods*, A**317**, 373–382.

Boeuf, A., Lagomarsino, S., Mazkedian, S., Melone, S., Puliti, P. & Rustichelli, F. (1978). *J. Appl. Cryst.* **11**, 442–449.

Cauchois, Y. (1932). *J. Phys.* **3**, 320.

Cooper, M. & Leake, J. A. (1967). *Philos. Mag.* **15**, 1201–1212.

Cooper, M., Leake, J. A. & Weiss, R. J. (1965). *Philos. Mag.* **12**, 797–800.

DuMond, J. W. M. (1933). *Rev. Mod. Phys.* **5**, 1–33.

Eisenberger, P. & Reed, W. A. (1972). *Phys. Rev. A*, **5**, 2085–2094.

Erola, E., Eteläniemi, V., Suortti, P., Pattison, P. & Thomlinson, W. (1990). *J. Appl. Cryst.* **23**, 35–42.

Eteläniemi, V., Suortti, P. & Thomlinson, W. (1989). Report BNL-43247. Brookhaven National Laboratory, Upton, NY, USA.

Fajardo, P., Honkimäki, V., Buslaps, T. & Suortti, P. (1998). *Nucl. Instrum. Methods*, B**134**, 337–345.

Johann, H. H. (1931). *Z. Phys.* **69**, 185–206.

Johansson, T. (1933). *Z. Phys.* **82**, 507–528.

Lienert, U. (1995). PhD thesis, University of Manchester, UK.

Loupias, G. & Petiau, J. (1980). *J. Phys. (Paris)*, **41**, 265–271.

Manninen, S., Paakkari, T. & Kajantie, K. (1974). *Philos. Mag.* **29**, 167–178.

Pattison, P., Suortti, S. & Weyrich, W. (1986). *J. Appl. Cryst.* **19**, 353–363.

Phillips, W. C. & Weiss, R. J. (1968). *Phys. Rev.* **171**, 790–800.

Sakurai, Y., Ito, H., Urai, T., Tanaka, Y., Sakai, N., Iwazumi, T., Kawata, H., Ando, M. & Shiotani, N. (1992). *Rev. Sci. Instrum.* **63**, 1190–1193.

Schulze, C. & Chapman, D. (1995). *Rev. Sci. Instrum.* **66**, 2220–2223.

Schulze, C., Suortti, P. & Chapman, D. (1994). *Synchrotron Rad. News*, **7**, 8–11.

Suortti, P., Chapman, D., Schneider, J. R. & Tschentscher, T. (1992). *J. Appl. Cryst.* **25**, 432–438.

Suortti, P., Lienert, U. & Schulze, C. (1994). *Nucl. Instrum. Methods*, A**338**, 27–32.

Suortti, P., Pattison, P. & Weyrich, W. (1986*a*). *J. Appl. Cryst.* **19**, 336–342.

Suortti, P., Pattison, P. & Weyrich, W. (1986*b*). *J. Appl. Cryst.* **19**, 343–352.

Suortti, P. & Thomlinson, W. (1988). *Nucl. Instrum. Methods*, A**269**, 639–648.

Weyrich, W. (1975). *Ber. Bunsenges. Phys. Chem.* **79**, 1085.

White, J. E. (1950). *J. Appl. Phys.* **21**, 855–859.